

## The Role of Sloping Sidewalls in Forming Potential Vorticity Contrasts in the Ocean Interior

RICHARD G. WILLIAMS AND VASSIL ROUSSENOV

*Oceanography Laboratories, Department of Earth Sciences, University of Liverpool, Liverpool, United Kingdom*

(Manuscript received 2 May 2002, in final form 6 August 2002)

### ABSTRACT

The role of sidewalls in determining the interior distribution of potential vorticity (PV) is investigated using eddy-resolving isopycnic experiments. The layer model is integrated at  $1/16^\circ$  resolution for a wind-driven double gyre with either vertical or sloping sidewalls. If there are vertical sidewalls, eddy stirring leads to PV homogenization within unforced, interior density layers. If there are sloping sidewalls, frictional torques lead to bands of low and high PV being formed along the western boundary of the subpolar and subtropical gyres, respectively. These regions of low and high PV are transferred into the interior by a separated jet at the intergyre boundary. Over a limited domain, this injection of the PV contrast can prevent eddy homogenization from occurring. However, over a larger-scale domain, eddies provide a downgradient transfer of PV, reducing the PV contrast downstream along the jet and enabling homogenization to occur for intermediate layers within the basin interior. Diabatic mixing along the slope can introduce low PV for intermediate layers and even mask the frictional contributions.

### 1. Introduction

Given the adiabatic nature of the interior ocean, the potential vorticity (PV) distribution is principally determined by a competition between PV sources from boundaries and stirring by geostrophic eddies. For example, over the upper thermocline, the PV distribution is controlled by a combination of ventilation from the diabatically forced, surface mixed layer and eddy stirring. In the deep ocean, fluid can become decoupled from the surface mixed layer for many years or decades. Consequently, ventilation might become less important in influencing the PV. Instead, frictional stresses and diabatic mixing associated with the sidewalls and above rough topography might become more important in determining the PV in the ocean interior.

Rhines (1998) first suggested that sloping sidewalls provide a boundary source of PV, which might be important for the ocean interior. Hallberg and Rhines (2000) investigated this process using numerical experiments to demonstrate how these boundary sources of PV are transferred into the ocean interior and, in some cases, prevent the homogenization of PV. In our study, we extend their experiments to higher resolution in order to investigate the mechanism by which sidewalls alter

the PV and assess its role in determining PV over the ocean interior.

The formulation of our model experiments are briefly reviewed in section 2 with details of the model version of the PV equation given in the appendix. Eddy-resolving experiments are conducted over a limited domain, including sensitivity studies investigating the role of the bottom drag and diapycnal mixing, which are described in section 3. The experiments are analyzed in terms of the adjustment of the density and PV distributions, as well as in terms of the change in the depth-integrated circulation. The larger-scale consequences of the process are addressed by extending the eddy-resolving experiments over a larger domain in section 4. The implications of the study are finally discussed in section 5.

### 2. Model formulation

#### *a. Model configuration*

The isopycnic code of Bleck and Smith (1990) (Miami Isopycnic Coordinate Ocean Model: MICOM 2.7) is adopted for a wind-forced double gyre either with vertical sidewalls or a sloping sidewall over the western boundary (Fig. 1). The model experiments are conducted at  $1/16^\circ$  degree resolution in the horizontal and 11 layers in the vertical in order to resolve the eddy structure and the sloping topography. Sensitivity experiments investigating the importance of the bottom drag and diapycnal mixing are conducted over an artificially re-

---

*Corresponding author address:* Dr Richard G. Williams, Oceanography Laboratories, Department of Earth Sciences, University of Liverpool, Liverpool, L69 7ZL, United Kingdom.  
E-mail: ric@liv.ac.uk

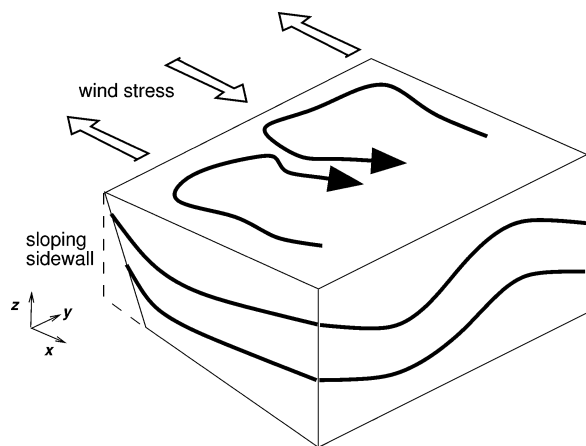


FIG. 1. A schematic figure for the model domain of a wind-forced double gyre within a basin. Experiments are performed with either a vertical or sloping sidewall along the western boundary. In the former case, bottom drag is only experienced in the bottom layer, whereas in the latter case, the drag is experienced within all the layers along the sidewall.

stricted domain extending  $6^\circ \times 6^\circ$  in the horizontal and 1500 m in the vertical (section 3). The larger-scale effect of sloping boundaries is investigated for an expanded domain of  $25^\circ \times 25^\circ$  in the horizontal and 3000 m in the vertical (section 4). The sloping sidewall has a constant slope of 0.6%, which extends to 250 km for the limited domain and 500 km for the extended domain.

The model is initialized with 10 layers of constant density and a surface mixed layer with a variable density. Each layer is initially 100 m thick, apart from the surface layer which is 450 m thick. The layers can acquire zero thickness with grounding on the seafloor or outcropping in the mixed layer permitted.

The surface layer is forced by a westerly wind stress varying sinusoidally with latitude over the domain,  $\tau_o \sin(\pi y/L)$ , where  $\tau_o = 0.1 \text{ N m}^{-2}$  and  $L$  is the north-south scale of the basin. A bottom drag is included with a quadratic dependence on bottom velocity and a bottom drag coefficient of  $c_d = 3 \times 10^{-3}$ . The bottom drag decreases linearly with height above the seafloor over a thickness of 10 m. No-slip boundary conditions are applied on the sidewalls. The momentum mixing is deformation dependent with a background Laplacian mixing and a turbulent mixing velocity of  $1 \text{ cm s}^{-1}$ . In the standard experiments, the only buoyancy forcing included is a biharmonic diffusion of thickness using a thickness diffusion velocity of  $0.5 \text{ cm s}^{-1}$ . The model experiments are integrated for 20 years for the limited domain and for 26 years over the extended domains. Time-mean diagnostics are applied to the last 10 years of integration.

### b. Potential vorticity

The model diagnostics focus on the distribution of PV, which is diagnosed here in terms of the absolute vorticity divided by the layer thickness  $h$ :

$$Q = \frac{\zeta + f}{h}, \quad (1)$$

where  $\zeta$  is the relative vorticity and  $f$  is the planetary vorticity. The PV plots are shown in terms of a stratification-scaled version,  $Q\Delta\sigma/\bar{\rho}$ , in order that the magnitude of the PV is comparable to that diagnosed from observations, where  $\Delta\sigma$  is the  $\sigma$  difference between layer interfaces and  $\bar{\rho}$  is a reference density.

This layered definition does lead to a singularity whenever  $h$  vanishes along a sidewall and contrasts with a definition based on continuous stratification as used in data analyses,  $-(f/\bar{\rho})\partial\sigma/\partial z$  (e.g., McDowell et al. 1982; O'Dwyer and Williams 1997).

The evolution of PV in the model is approximately given by (see the appendix)

$$\frac{DQ}{Dt} = -\frac{g}{h} \frac{\partial}{\partial p} (\mathbf{k} \cdot \nabla \times \boldsymbol{\tau}) + \frac{\nu}{h} \nabla^2 \zeta - \frac{QB}{h}. \quad (2)$$

Hence, the Lagrangian evolution of PV is controlled by (i) a vertical divergence in the frictional torque, (ii) a lateral diffusion of vorticity, and (iii) buoyancy forcing; here  $D/Dt \equiv \partial/\partial t + \mathbf{u} \cdot \nabla$  is the substantial derivative,  $B$  is the buoyancy forcing,  $g$  is gravity,  $\mathbf{k}$  is a unit vertical vector,  $p$  is the pressure,  $\mathbf{u}$  is the horizontal velocity vector,  $\boldsymbol{\tau}$  is the stress, and  $\nu$  is the diffusivity of momentum.

### 3. Model experiments over a limited domain

For the limited domain, eddy-resolving experiments are integrated with vertical or sloping sidewalls. Sensitivity experiments with sloping sidewalls are also conducted using different values of bottom drag and diapycnic mixing.

#### a. Density structure

The wind forcing provides the expected gyre-scale undulations of isopycnals, which are depressed over the subtropical gyre and elevated over the subpolar gyre (Fig. 2). When sloping sidewalls are incorporated, the bottom stress is experienced in each layer intersecting the boundary. The bottom stress drives upslope and downslope Ekman flows over the western boundary of the subtropical and subpolar gyres respectively. Accordingly, the layer thickness becomes thin over the western boundary for the subtropical gyre and thick over the subpolar gyre (Fig. 2). This Ekman transport is carried within the layer adjacent to the solid boundary, although the model resolution of 11 layers is generally insufficient to resolve this process within a thin, bottom boundary layer.

The resulting thermal-wind adjustment along the boundary acts to reduce the bottom velocity, as partly seen over the western boundary of the subtropical gyre (Fig. 2, shading). This response should act to make the bottom flow vanish and the bottom boundary layer be-

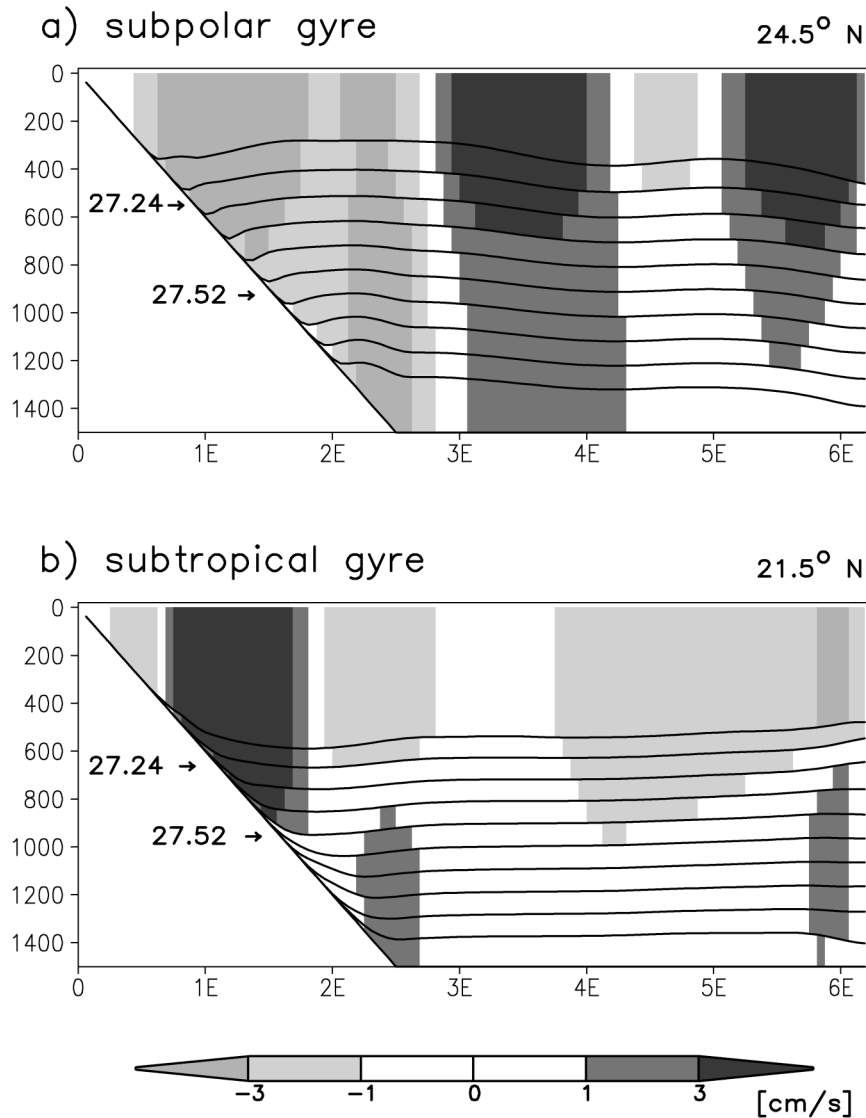


FIG. 2. West-east sections for the model experiment with a sloping sidewall showing layer interfaces through (a) the subpolar gyre and (b) the subtropical gyre. The sign of the meridional velocities is denoted by shading for magnitudes greater than  $1 \text{ cm s}^{-1}$  (the surface velocities reach  $10\text{--}15 \text{ cm s}^{-1}$ ). The Ekman pumping depresses the layer interfaces over the subtropical gyre and uplifts the interfaces over the subpolar gyre. Along the sloping sidewall, the interfaces become more normal to the slope over the subpolar gyre, whereas they are uplifted over the subtropical gyre. Subsequent diagnostics focus on the PV in an upper layer ( $\sigma = 27.24$ ) and a deeper layer ( $\sigma = 27.52$ ), which are the ninth and fifth layers above the seafloor, respectively, as marked by the arrows.

come “slippery” (MacCready and Rhines 1993; Garrett et al. 1993). The model integration of 10 years is longer than the estimated shut down timescale of  $S^{-1}f^{-1}$  (Garrett et al. 1993), which is typically on the order of 1 month where  $S = N^2 \sin^2 \theta / f^2$  is the Burger number based on the angle of slope  $\theta$ , and here  $N \sim 10^{-3} \text{ s}^{-1}$ ,  $f \sim 10^{-4} \text{ s}^{-1}$ , and  $\theta = 3^\circ$ . This shut down timescale might be artificially long in the model because of the coarse vertical resolution: interestingly, there is more velocity shear over the slope in the subtropical gyre where the layers are thinner than in the subpolar gyre

(Fig. 2b). In our model integrations, any local adjustment does not dominate over the larger-scale forcing, which generates an active eddy field maintaining a deep circulation (Rhines and Holland 1979).

*b. Potential vorticity*

1) VERTICAL SIDEWALLS

When there are vertical sidewalls, frictional torques from the wind stress and bottom friction are confined

to the top and bottom layers. For the intermediate layers, there is only a weak lateral diffusion of vorticity and a biharmonic dissipation of thickness.

The wind stress forcing drives the expected cyclonic and anticyclonic circulations over the subpolar and subtropical gyres respectively (Fig. 3a, contours). Accordingly, for each layer, the wind forcing increases the vorticity over the subpolar gyre and decreases it over the subtropical gyre (Fig. 4a, upper panel). In the bottom layer, the bottom drag opposes the vorticity input from the surface wind forcing, injecting anticyclonic vorticity over the subpolar gyre and cyclonic vorticity over the subtropical gyre. The horizontal convergence of the surface Ekman transport decreases the thickness of the surface layer over the subpolar gyre and increases it over the subtropical gyre. Conversely, the convergence of the bottom Ekman transport increases the thickness of the bottom layer over the subpolar gyre and decreases it over the subtropical gyre.

When there are vertical sidewalls, the PV is only altered through the external forcing from the divergence of the stress over the surface and bottom layers (2). Hence, the wind forcing increases the PV over the surface layer for the subpolar gyre and decreases it over the subtropical gyre with the contributions from the vorticity and thickness changes reinforcing each other. Over the intermediate layers, there is no direct forcing of PV with the changes in vorticity and thickness compensating each other (Fig. 4a). Bottom friction is confined to the bottom layer where PV is decreased over the subpolar gyre and increased over the subtropical gyre.

The eddy stirring redistributes the PV within each layer with PV gradients expelled towards the northern and southern boundaries (Fig. 3a, shading). The PV is homogenized within closed geostrophic contours in the intermediate layers, as expected from homogenization theory (Rhines and Young 1982).

## 2) SLOPING SIDEWALLS

When sloping sidewalls are introduced, each layer experiences a bottom drag where the layer intersects the sidewall. Accordingly, the vorticity input by the bottom drag is now spread over all layers intersecting the boundary, rather than confined to a single layer over the seafloor. As before, this frictional input of vorticity acts to oppose the input from the wind, forming bands of anticyclonic vorticity and cyclonic vorticity along the western boundary of the subpolar and subtropical gyres respectively (Fig. 4b, upper panel). Concomitant with this vorticity input, the layer thickness becomes thick and thin over the western flanks of the subpolar and subtropical gyres respectively (Figs. 2 and 4b, middle panels).

The frictional torque along the sloping sidewall introduces bands of low and high PV along the western boundary of the subpolar and subtropical gyres respectively (Figs. 3b and 4b). The changes in vorticity and

layer thickness reinforce each other over a narrow boundary zone (extending to  $1^\circ\text{E}$ ), but oppose each other farther into the interior (Fig. 4b). The PV contrasts are advected into the interior by a separated jet at the intergyre boundary. This transfer of PV makes the intermediate layers have higher PV over the subtropical gyre and lower PV over the subpolar gyre, which is in the opposite sense to the vorticity input from the wind.

The transfer of PV from the sloping boundary into the interior varies with the strength of the circulation. Over upper layers, the jet is sufficiently strong to transfer the PV contrasts from the sloping boundary into the interior (Figs. 3b and 4b). Hence, over this limited domain, the eddy-induced homogenization of PV is inhibited. However, over the deeper layers, the jet is weaker, the PV contrasts are confined to the sloping boundary, and the eddy homogenization process again dominates in the interior (see later Fig. 7a, right panel).

In addition to the action of the boundary torques, the layer thickness becomes small along the sidewall where the water column thins, which introduces a singularity of high PV (Figs. 3b and 4b, occurring farther onshore of the dashed line denoting where the bottom layer is less than 10 m thick).

## c. Diagnostics of the PV budget

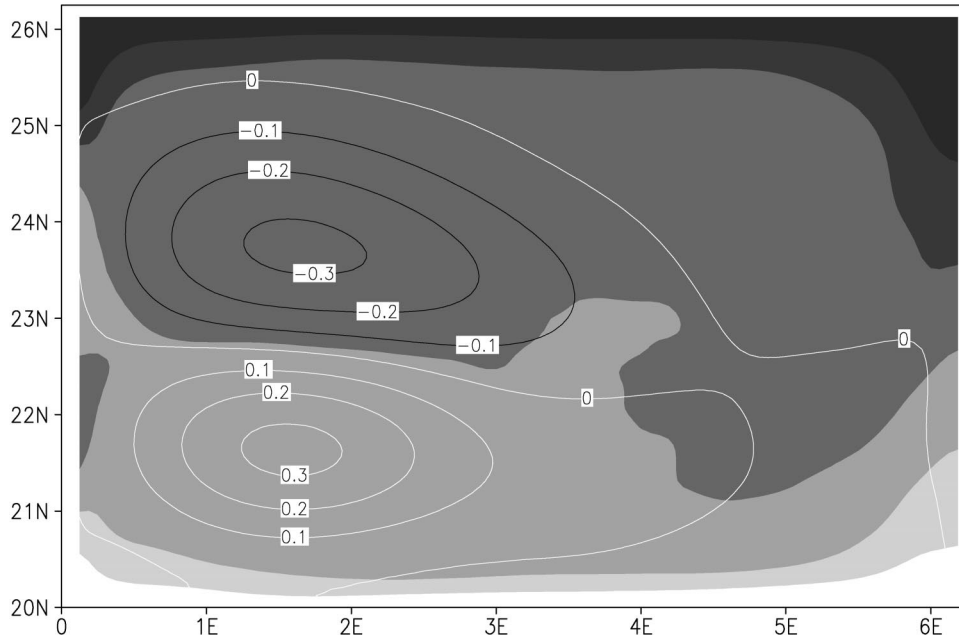
First, the change in PV is evaluated in a Lagrangian frame following time-mean streamlines around each gyre in order to confirm how the PV signals are formed. Since a time-mean streamline is followed, the PV balance (2) is extended to include an explicit eddy transfer of PV anomalies. In this case, the dominant forcing terms are from the frictional torques and the eddy advection of PV anomalies:

$$\left(\frac{\partial}{\partial t} + \bar{\mathbf{u}} \cdot \nabla\right) Q \approx -\frac{g}{h} \frac{\partial}{\partial p} (\mathbf{k} \cdot \nabla \times \boldsymbol{\tau}) - \overline{\mathbf{u}' \cdot \nabla Q'}, \quad (3)$$

where the overbar represents an Eulerian time average and a prime represents a temporal deviation. The eddy transfer of PV,  $\overline{\mathbf{u}' \cdot \nabla Q'}$ , is diagnosed directly at each grid point from the model diagnostics over a 2-yr time average and has positive and negative values along the separated intergyre jet.

The PV evolution is assessed following a fluid parcel as it follows a 120-day circuit along a time-mean streamline over each gyre, which is evaluated from a 2-yr, time average (Fig. 5a). For the subpolar gyre, the PV decreases along the western boundary during the first 20 days and then subsequently increases and decreases downstream over the interior (Fig. 5b, full line). The decrease in PV along the western boundary is due to the frictional torque, which is partly opposed by the eddy diffusion of PV (3) (Fig. 5b, long and short dashed lines, respectively). The downstream increase and decrease in PV is due to changing sign of the eddy transfer of PV.

a) vertical wall



b) sloping wall

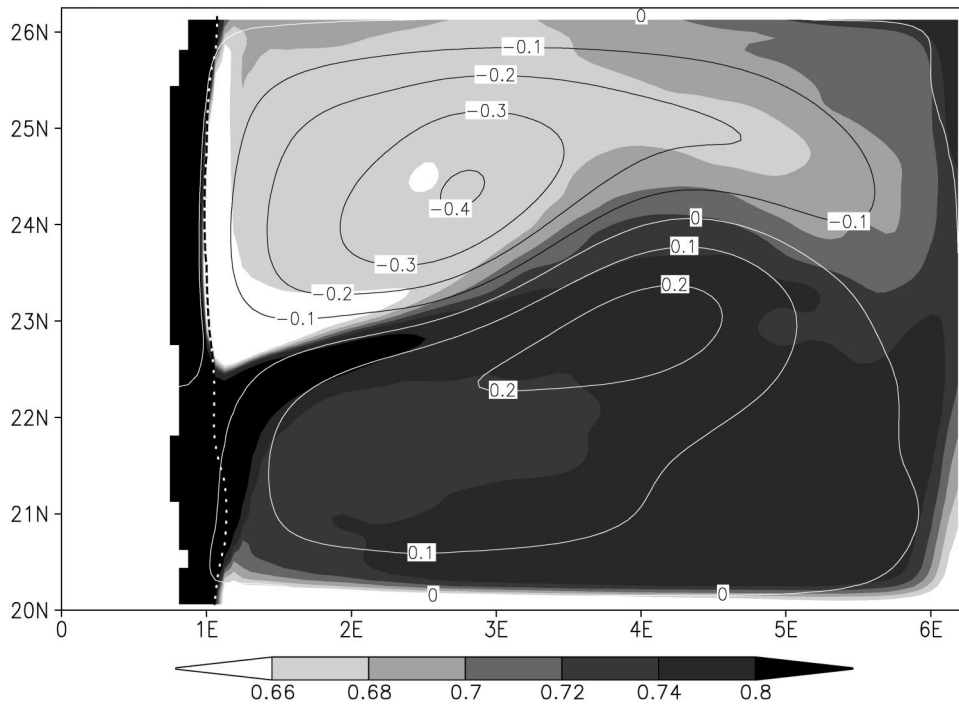


FIG. 3. Plan views of the time-mean streamfunction (contours: Sv; 1 Sv  $\equiv 10^6 \text{ m}^3 \text{ s}^{-1}$ ) and PV (shaded) ( $10^{-10} \text{ m}^{-1} \text{ s}^{-1}$ ) in the upper layer ( $\sigma = 27.24$ ) for (a) vertical and (b) sloping sidewalls. The PV distribution is relatively uniform in (a), whereas there is higher PV over the subtropical gyre and lower PV over the subpolar gyre in (b).

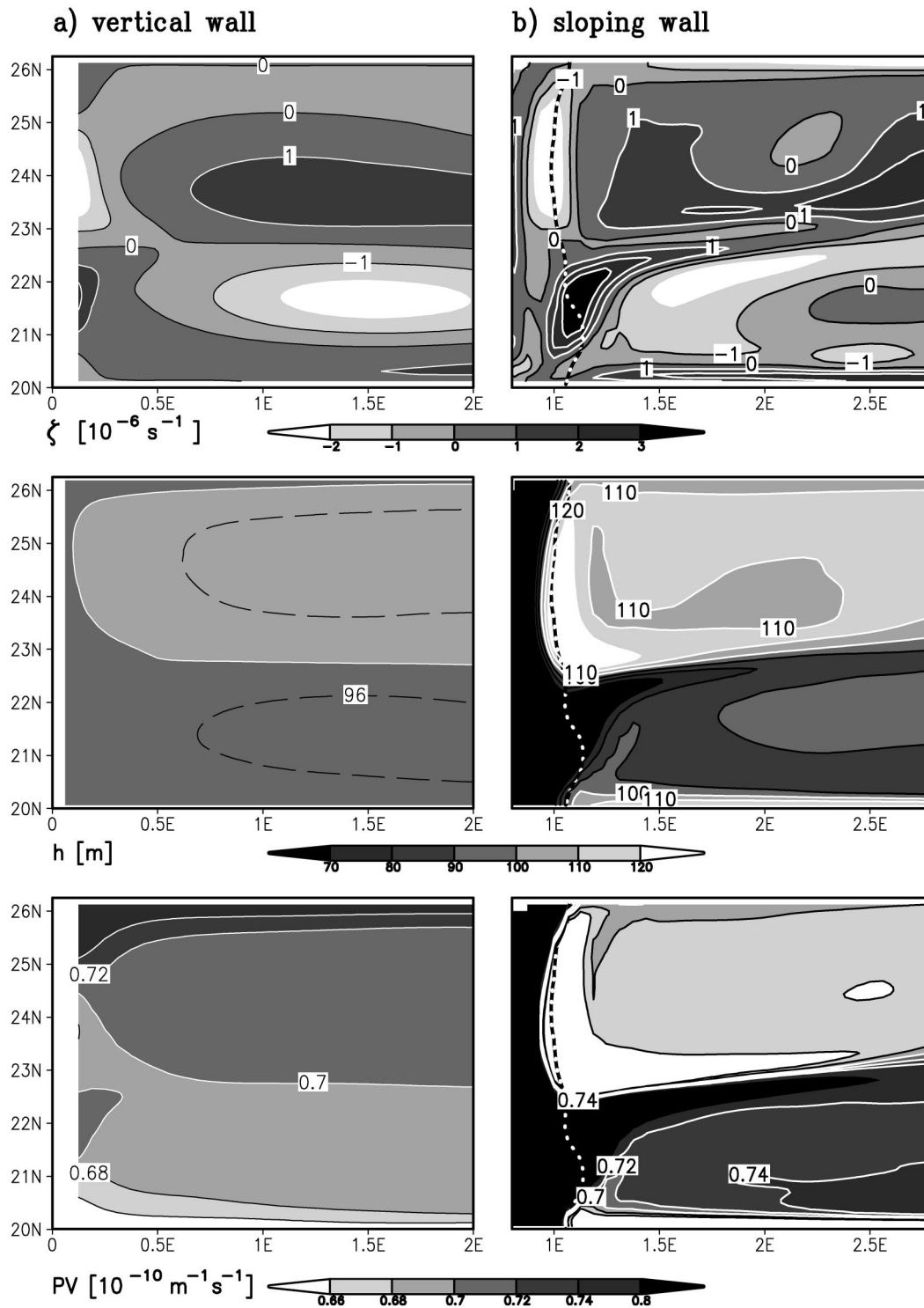


FIG. 4. Plan views for (a) vertical and (b) sloping sidewalls of the relative vorticity ( $10^{-6} \text{ s}^{-1}$ ), layer thickness (m), and PV ( $10^{-10} \text{ m}^{-1} \text{ s}^{-1}$ ) in the upper layer ( $\sigma = 27.24$ ) over the western part of the basin.

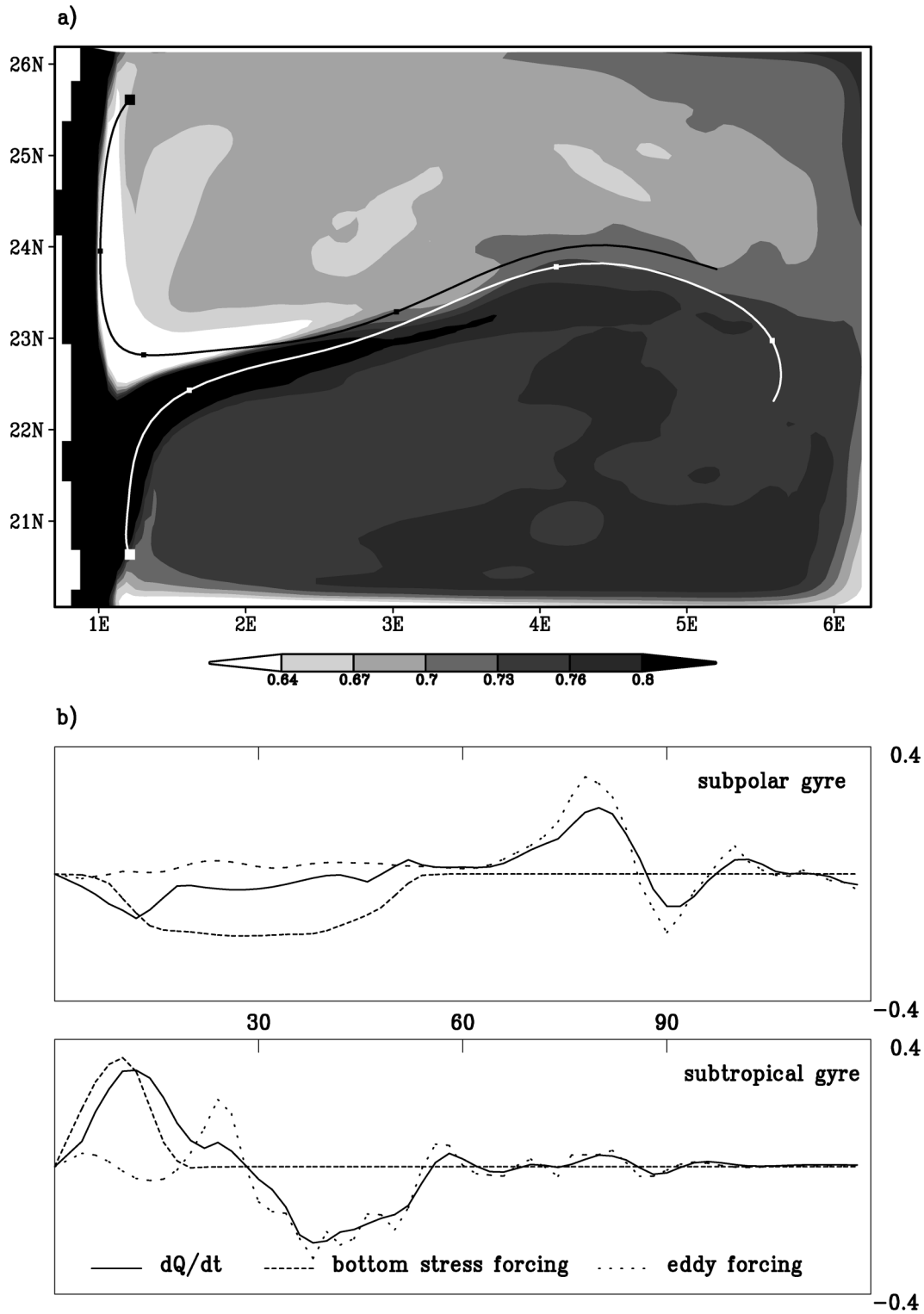


FIG. 5. The evolution of PV following a time-mean streamline for the upper layer with a sloping sidewall in the subpolar gyre and the subtropical gyre: (a) a plan view of the PV (shaded) ( $10^{-10} \text{ m}^{-1} \text{ s}^{-1}$ ) and two trajectories following time-mean streamlines. The 120-day-long trajectories used to evaluate the PV change over each gyre are included with the start point and positions every 30 days marked by large and small squares, respectively. The change in PV,  $DQ/Dt$ , (full line), the curl of the bottom drag (closely spaced dashed line) and the eddy diffusion of  $Q$ ,  $\bar{\mathbf{u}}' \cdot \nabla' Q'$ , (widely spaced dashed line) are shown following streamlines in the subpolar and subtropical gyres. Units are  $10^{-16} \text{ m}^{-1} \text{ s}^{-2}$ .

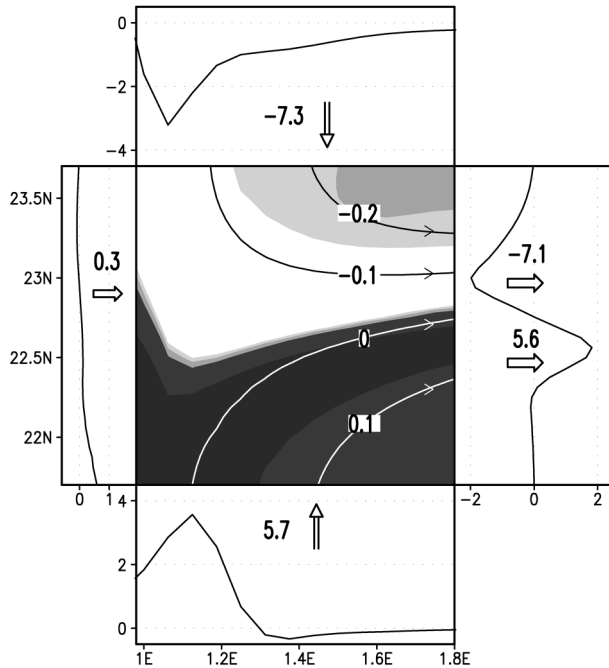


FIG. 6. An integrated PV flux budget is diagnosed for the upper layer over a central part of the domain where the midbasin jet leaves the slope. There are low and high PV plumes originating from the subpolar and subtropical gyres respectively, as shown in the expanded plan view of the PV ( $10^{-10} \text{ m}^{-1} \text{ s}^{-1}$ ) in the center panel with the shading as in Fig. 5, together with time-mean streamlines (Sv). The integrated PV flux for the layer through each face of the box ( $10^{-6} \text{ m}^2 \text{ s}^{-2}$ ) is evaluated as  $\int |\mathbf{u} \cdot \mathbf{n}| (Q - Q^*) h ds$ , where  $\mathbf{u} \cdot \mathbf{n}$  is the velocity through the face of the box,  $\mathbf{n}$  is a unit normal vector,  $ds$  is a distance element, and  $Q^* = \overline{Qh}/\overline{h}$  is the thickness-weighted mean PV for the layer within the box. On the side panels, the numbers denote the magnitude of the integrated PV flux for the layer through each side of the box, the arrows denote the direction of the flux, and the sign reflects whether a positive or negative PV anomaly is introduced. In addition, the curves show this anomalous thickness-weighted PV flux per unit length ( $10^{-10} \text{ m s}^{-2}$ ). On the eastern face, the budget is separately evaluated for the high and low PV plumes.

For the subtropical trajectory, the PV increases along the western boundary during the first 30 days, decreases in the interior from days 30 to 60, and then remains relatively constant over the remainder of the circuit (Fig. 5b, full line). The increase in PV is achieved through the frictional torque over the western boundary and the decrease in PV from the eddy diffusion of PV.

Second, in order to clarify whether the western edge region of high PV is important, an integrated PV flux budget is applied over the central part of the domain ( $21.7\text{--}23.7^\circ\text{N}$ ,  $1.0\text{--}1.8^\circ\text{E}$ ). The PV distribution over the midjet region reveals plumes of low and high PV originating from the slope over the subpolar and subtropical gyres respectively, as shown in Fig. 5a and an enlargement in the central panel of Fig. 6. The integrated PV flux for the layer through each face of the box is evaluated as  $\int |\mathbf{u} \cdot \mathbf{n}| (Q - Q^*) h ds$ , where  $\mathbf{u} \cdot \mathbf{n}$  is the velocity through the face of the box,  $\mathbf{n}$  is a unit normal vector,  $ds$  is a distance element, and  $Q^* = \overline{Qh}/\overline{h}$  is the

thickness-weighted mean PV for the layer within the box. The integrated fluxes of high and low PV through the southern and northern faces closely match those fluxes passing out of the eastern face: as shown by the numbers marked on the side panels of Fig. 6, where the sign reflects whether the PV anomaly is positive or negative, the arrows denote the direction of the flow, and the curves show the integrated PV flux per unit length. In contrast, the integrated PV flux is relatively small from the western wall where there is the high PV singularity and does not explain the plume of high PV passing through the eastern face.

Consequently, from the diagnosed PV changes following a time-mean streamline and the integrated PV flux diagnostics, the high PV associated with the vanishing in layer thickness along the western edge of the domain is comparatively unimportant in determining the interior PV distribution. The plume of high PV entering the interior is formed predominately through a frictional torque over the subtropical gyre, rather than an eddy transfer of high PV from the edge region, and there is an accompanying plume of low PV from the subpolar gyre.

#### d. Bottom drag

Given the importance of the bottom drag in the PV diagnostics following a time-mean streamline, the model experiments are repeated with the drag coefficient increased by a factor of 4 from  $c_d = 3 \times 10^{-3}$  to  $1.2 \times 10^{-2}$ . As expected, for an increased bottom drag, the PV contrasts are increased along the western boundary for both upper and deeper layers (Fig. 7). This enhanced PV contrast is again transferred into the gyre interior for the upper layer, increasing the PV over the subtropical gyre and decreasing it over the subpolar gyre, and hence inhibiting any homogenization of PV. Consequently, the bottom drag appears to control the formation of the PV contrasts along the sidewalls.

There are contrasting responses to a change in the lateral boundary condition if there are vertical or sloping sidewalls. In the vertical sidewall case, employing no slip leads over the western boundary to weak inputs of anticyclonic vorticity for the subpolar gyre and cyclonic vorticity for the subtropical gyre (Fig. 4a, left panel). These inputs of vorticity disappear when a free slip boundary condition is employed. In the sloping sidewall case, the model solution appear to be relatively insensitive to a change in the lateral boundary condition from no slip to free slip. This lack of sensitivity is due to the bottom friction in each layer along the sidewall masking any effect of the implied change in lateral transfer of vorticity.

#### e. Diapycnic mixing

The role of diapycnic mixing is now investigated over the sloping boundary given observations of enhanced

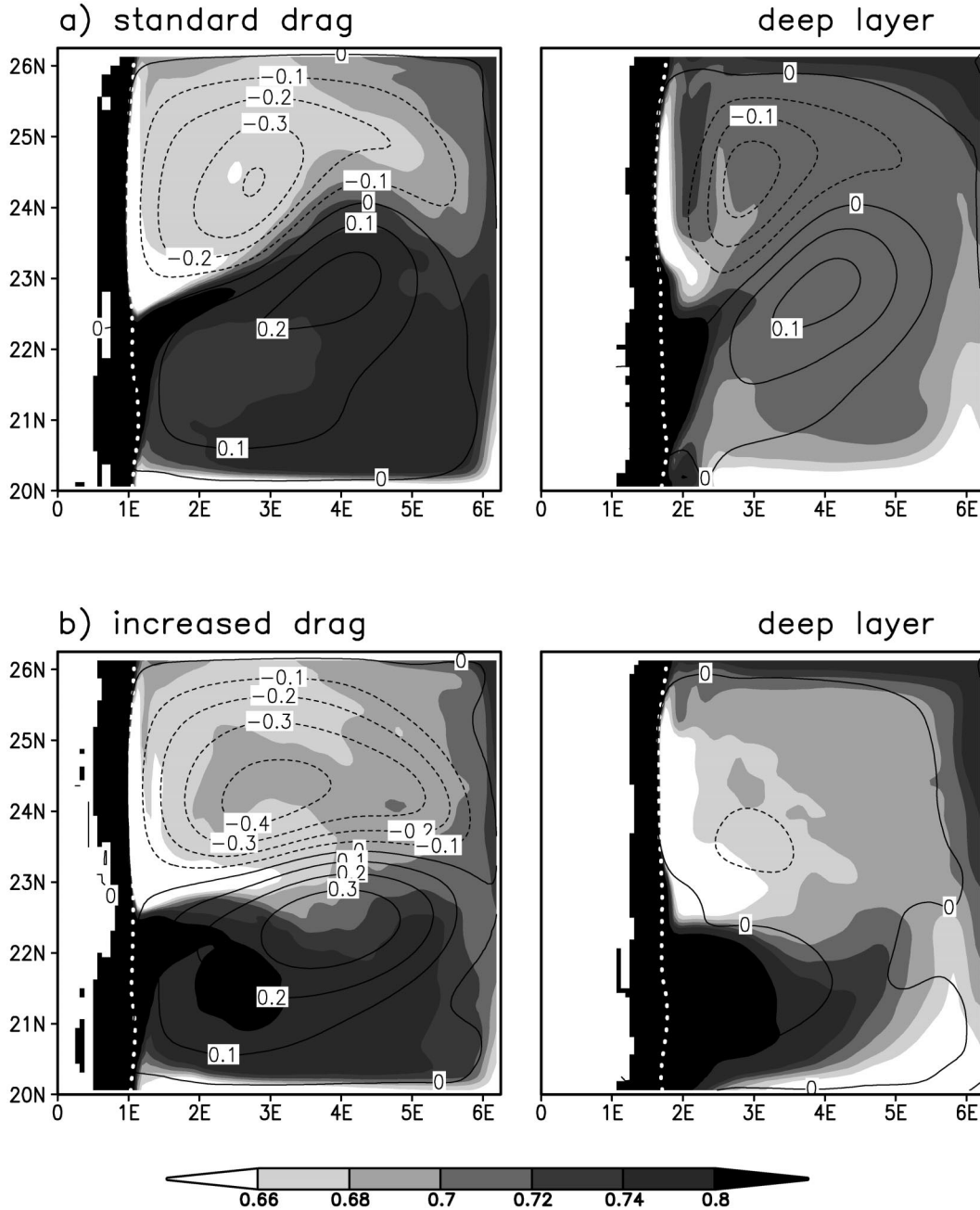


FIG. 7. Plan views of the time-mean PV (shaded) ( $10^{-10} \text{ m}^{-1} \text{ s}^{-1}$ ) and layer streamfunction (contours:  $S_v$ ) with sloping sidewalls for the (left) upper and (right) deeper layers for (a) standard value of bottom drag,  $c_d = 0.003$ , and (b) an increased bottom drag,  $c_d = 0.012$ . In the higher-drag case, larger PV contrasts are induced between the subtropical and subpolar gyres.

mixing over boundaries (Armi 1978) and above rough topography (Polzin et al. 1997). The diapycnic mixing is introduced over the slope, after 10 years of the standard model integration, and integrated for a further 10 years with diagnostics performed for a time mean over the last 2 years. The diffusivity is chosen to vary inversely with buoyancy frequency following Gargett (1984) with  $\kappa = 5 \times 10^{-7} \text{ m}^2 \text{ s}^{-2}/N$ , giving a local

value of  $\kappa \sim 5 \times 10^{-4} \text{ m}^2 \text{ s}^{-1}$  for  $N \sim 10^{-3} \text{ s}^{-1}$ . The diapycnal mixing is introduced as a volume flux at the interface between the two most dense layers above the topography, and hence is applied at all the interfaces intersecting the sloping sidewall and is restricted to the interface between the bottom two layers where the seafloor is flat. In order to conserve the volume of each layer and prevent a drift in the model, this local dia-

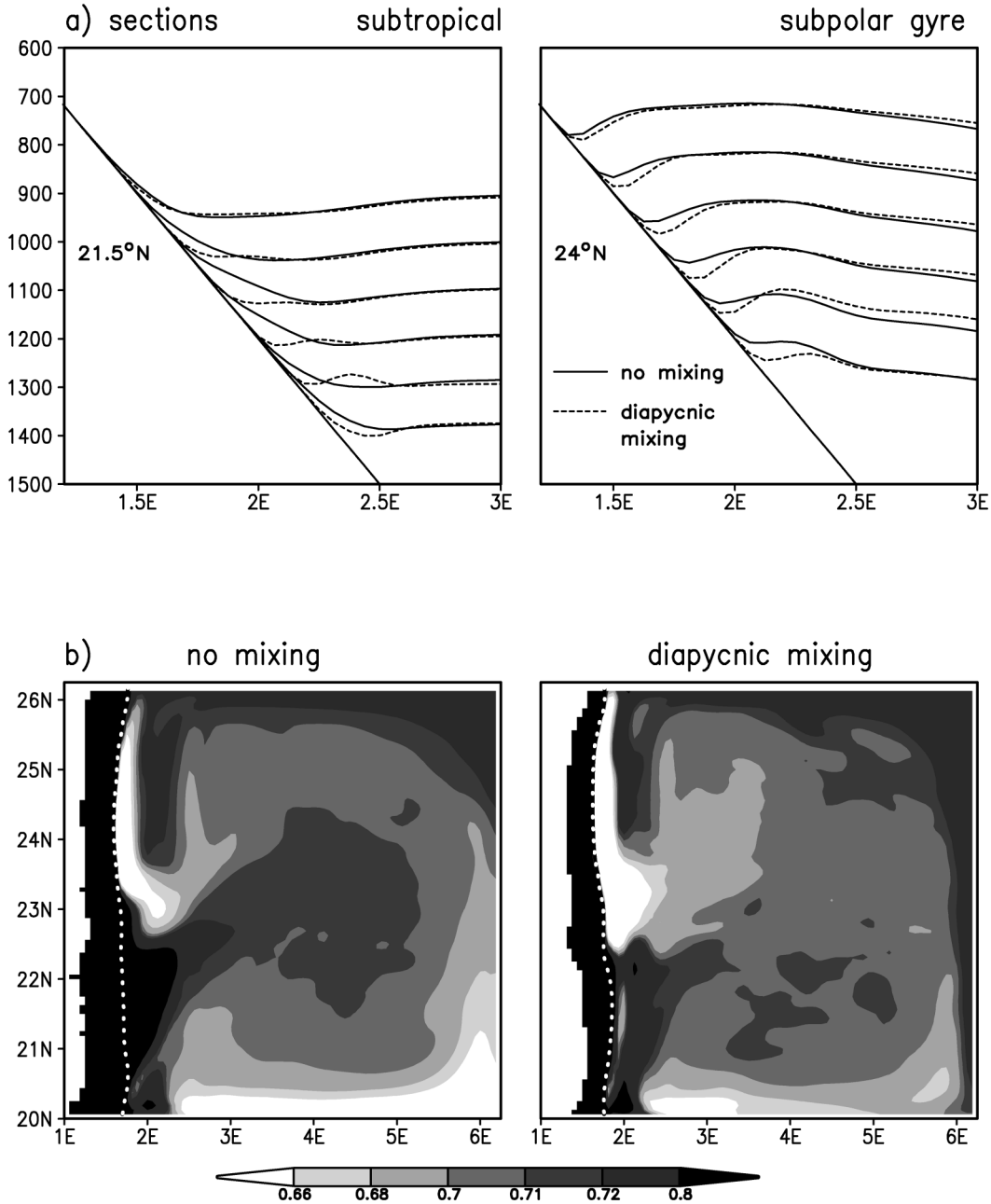


FIG. 8. (a) West-east section of interface height over the slope for the subtropical and subpolar gyres in experiments without and with diapycnic mixing (full and dashed lines, respectively) over the sloping boundary. (b) Plan views of the time mean PV ( $10^{-10} \text{ m}^{-1} \text{ s}^{-1}$ ) in a deep layer ( $\sigma = 27.52$ ). When there is diapycnic mixing, the PV is reduced in magnitude over much of the western boundary. The white dashed line denotes where the bottom interface of the layer intersects the slope.

pycnal flux is compensated for by an opposing diapycnal flux applied over the rest of the domain. This procedure mimics the action of external buoyancy forcing in introducing density contrasts, while allowing the local effects of the enhanced diabatic mixing to be investigated.

Introducing the mixing leads to an upslope diapycnal volume flux and interfaces being depressed along the sidewall (Fig. 8a, dashed lines), as first proposed by

Phillips (1970) and Wunsch (1970). Within an intermediate layer, the mixing generally introduces a lower PV along the boundary (Fig. 8b, right panel). In particular, the mixing leads to lower PV over the western flank of the subtropical gyre, where there had previously been a band of high PV formed through the frictional torque there. However, some of the changes are also an indirect consequence of changes in the circulation. For

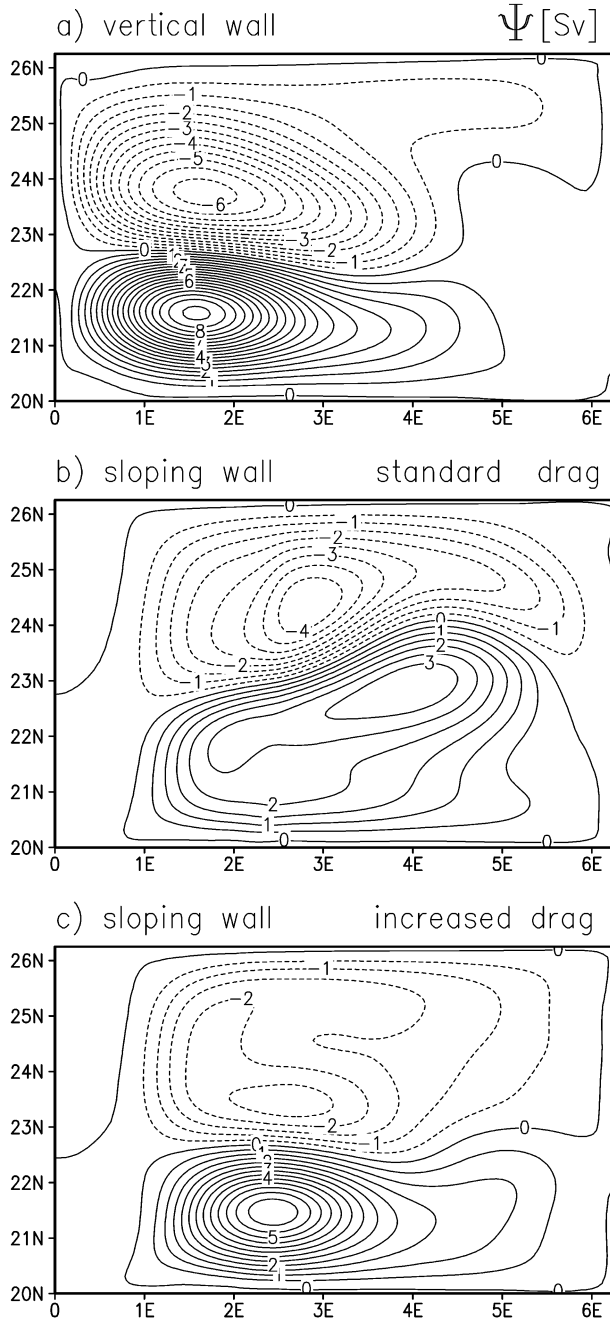


FIG. 9. Plan views of the depth-integrated transport streamfunction (Sv) for (a) vertical sidewalls and (b) a sloping sidewall with a standard bottom drag,  $c_d = 0.003$ , and (c) a sloping sidewall with an increased bottom drag,  $c_d = 0.012$ . The change in topography and bottom friction alters the streamfunction with a symmetric pattern in (a) and the most asymmetric pattern in (b).

example, the greater southward extent of the low PV plume along the western boundary from the subpolar gyre is due to a stronger southward advection within this particular layer. In summary, the diapycnal mixing can modify the PV over the boundary and even mask the contribution of the frictional stresses.

f. Barotropic response

In these different model integrations, as well as the changes in PV distribution, there are changes in the circulation pattern. For vertical sidewalls, the wind forcing drives a classical, symmetric double-gyre circulation (Fig. 9a). Incorporating sloping sidewalls adjusts the depth-integrated streamfunction with the separation point moving southward. The subpolar gyre extends farther to the southwest and the subtropical gyre farther to the northeast (Fig. 9b). This solution has a similar character to the analytical solutions of Salmon (1994) and Ford (2000) with sloping sidewalls. Increasing the bottom drag reduces this asymmetry between the subtropical and subpolar gyres with a more zonal jet and the separation point returning northward (Fig. 9c).

These change in the circulation may be understood in terms of the vorticity balance for the depth-integrated flow. Following Mertz and Wright (1992), depth integrating the linearized momentum equations and cross-differentiating gives

$$\frac{\partial}{\partial t} \nabla^2 \psi + \beta \frac{\partial \psi}{\partial x} = \frac{1}{\rho_o} J(P_b, H) + \frac{1}{\rho_o} \text{curl}_z(\tau_s - \tau_b). \quad (4)$$

The time evolution of the vorticity of the depth-integrated flow plus the transport across planetary vorticity contours,  $\beta \partial \psi / \partial x$ , balances the bottom pressure topographic torque,  $J(P_b, H)$ , and the curl of the frictional stresses; here  $\psi$  is the streamfunction of the depth-integrated flow,  $P_b$  is the bottom pressure,  $\beta$  is the meridional gradient in the Coriolis parameter,  $H$  is the fluid depth,  $\rho_o$  is a reference density,  $\tau_s$  and  $\tau_b$  are the surface and bottom stresses, and

$$J(A, B) \equiv \frac{\partial A}{\partial x} \frac{\partial B}{\partial y} - \frac{\partial B}{\partial x} \frac{\partial A}{\partial y}.$$

In our model integrations with sloping topography, the dominant balance is between  $\beta \partial \psi / \partial x$  and  $J(P_b, H)$  over the sloping sidewalls, also obtained in global circulation model diagnostics by Hughes and de Cuevas (2001). Over the midpoint of the western boundary,  $J(P_b, H)$  is negative leading to the southward movement of the separation point (Fig. 10a, shading). When the bottom drag is increased, this southward movement of the separation point is decreased (Figs. 9b,c), as well as the bottom velocity decreased (Fig. 10a, contours). However, this change in the separation point is not directly due to the increased damping of vorticity (4). Instead the increased drag alters the density distribution with increased upward and downward tilt of the isopycnals across the slope for the subtropical and subpolar gyres respectively (Fig. 10b). This change in density distribution shifts the pattern of  $J(P_b, H)$  and hence the position of the separation point northward.

4. Model experiments over an extended domain

In order to assess the larger-scale relevance of the sidewall control of the PV, we extend our experiments

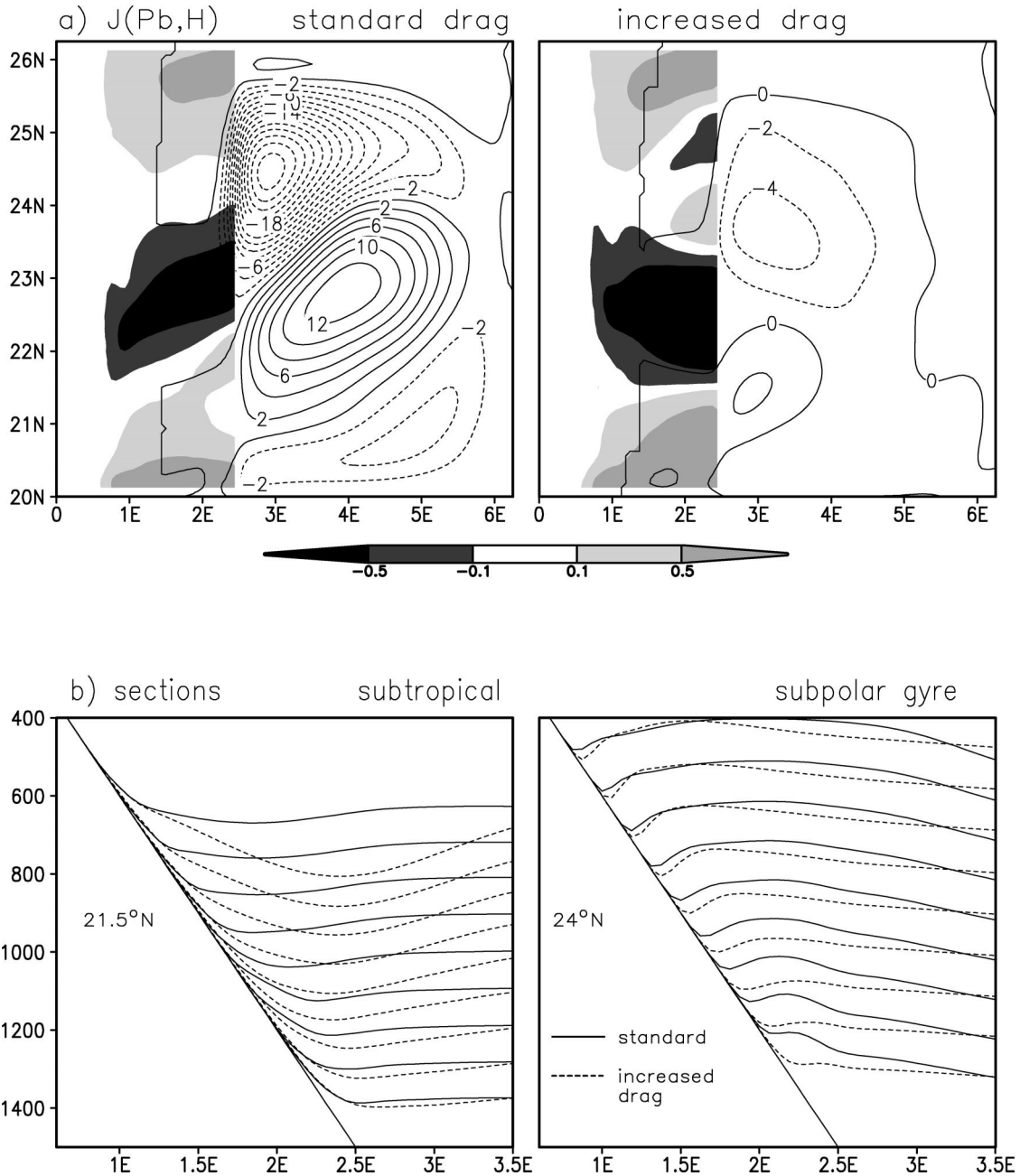


FIG. 10. (a) Diagnostics of the bottom pressure torque  $\rho_o^{-1}J(P_b, H)$  ( $10^{-9} \text{ m s}^{-2}$ ) (shaded up to  $2.5^\circ\text{E}$ ) over the sloping sidewall for standard and high values of the bottom drag together with the bottom layer streamfunction (contours:  $10^{-2} \text{ Sv}$ ). (b) Zonal sections showing density interfaces are included across the subtropical and subpolar gyres for the standard and high values of the bottom drag (full and dashed lines, respectively).

to a larger domain:  $25^\circ \times 25^\circ$  in the horizontal and 3000 m in the vertical, and the sloping sidewall extends for 500 km with its slope as 0.6%. The model is integrated for 26 years and the diagnostics performed over the last 10 years.

Larger PV contrasts are introduced across the basin given the larger change in planetary vorticity, compared with the previous limited domain. When there are ver-

tical sidewalls, the PV contrasts are again weak around the separated jet with PV contours expelled toward the flanks of the subtropical and subpolar gyres (Fig. 11a). The homogenization is not as striking as in the limited area case because of a longer time required to homogenize the PV given its larger initial contrast across the basin.

When there are sloping sidewalls, the frictional

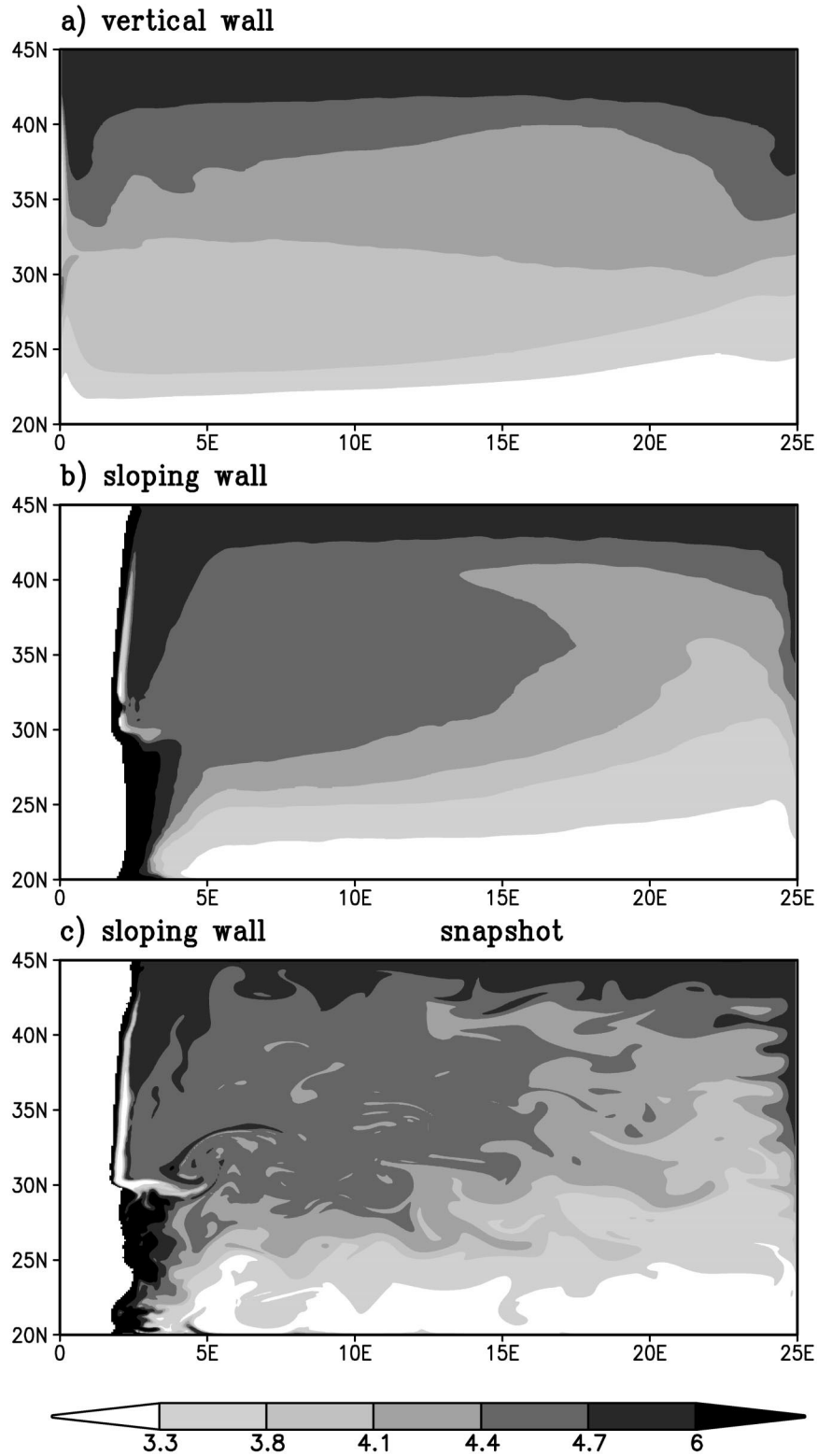


FIG. 11. Potential vorticity distributions for model experiments with an expanded domain of  $25^\circ \times 25^\circ$ . Plan views of the time mean PV ( $10^{-10} \text{ m}^{-1} \text{ s}^{-1}$ ) in an upper layer ( $\sigma = 27.57$ ) for (a) vertical and (b) sloping sidewalls. (c) A snapshot of the PV is shown for the sloping sidewall case in the last year of integration.

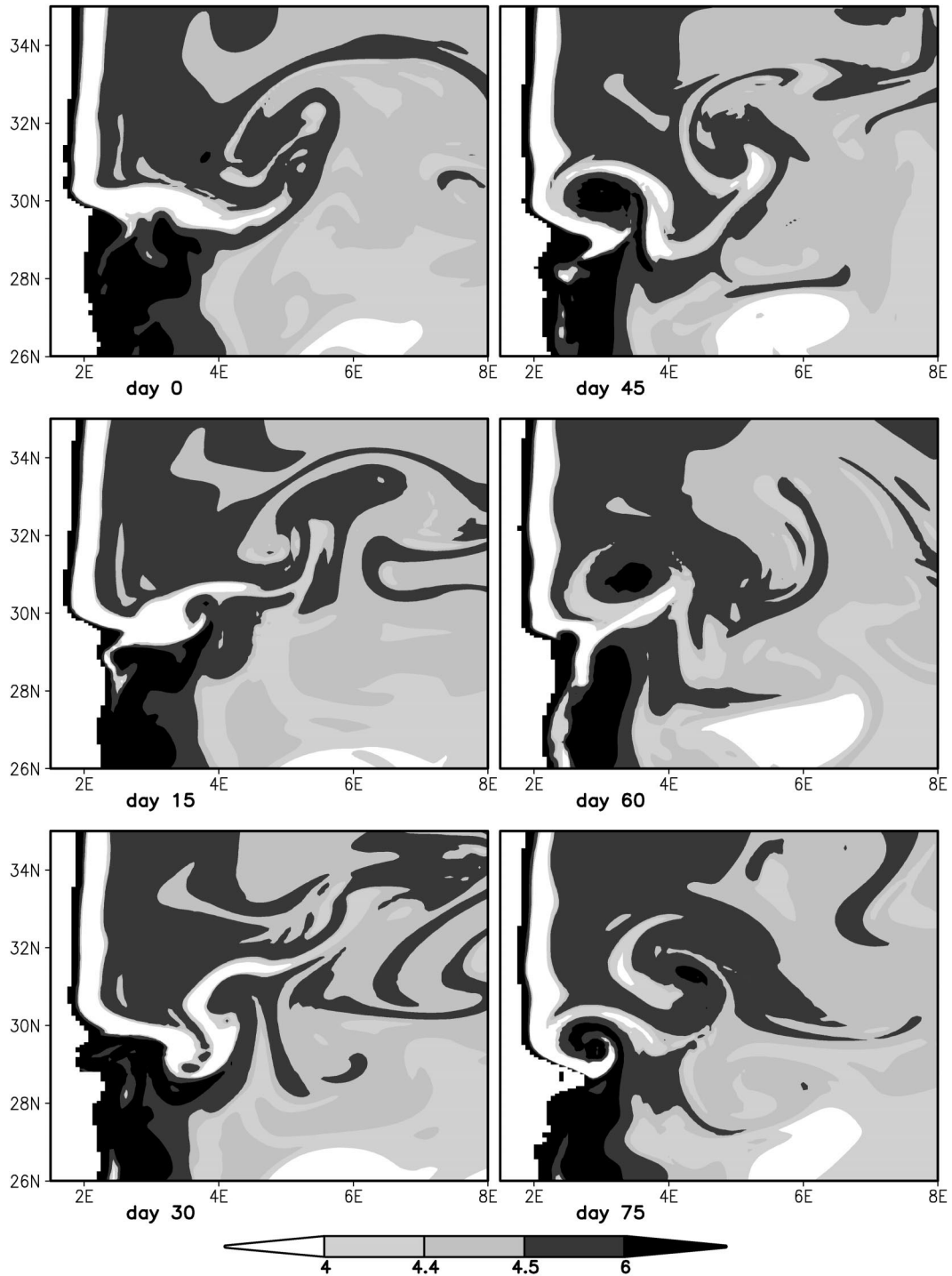


FIG. 12. A series of snapshots of the PV ( $10^{-10} \text{ m}^{-1} \text{ s}^{-1}$ ) over the western part of the basin for the experiment with a slope and an expanded domain of  $25^\circ \times 25^\circ$ . The snapshots are every 15 days from day 0 to 75, where day 0 starts from the snapshot shown in Fig. 11c during the last year of the integration.

torques again form bands of low and high PV along the sloping boundary (Fig. 11b). The separated jet advects these PV contrasts into the interior ocean. However, this boundary process does not now control the PV distri-

bution over the basin interior. Instead the PV contrast associated with the separated jet only extends up to  $5^\circ$ , rather than penetrating over the whole basin. The more restricted extent of this PV contrast appears to be due

to eddies progressively eroding the PV contrast downstream along the jet. In addition, over the interior, the gyre-scale circulation advects opposing signals of high PV from the northern wall and low PV from the southern wall. Consequently, in this experiment, the combination of these processes appears to limit the role of the boundary torques in determining the PV over a subregion of comparable width to the sloping boundary.

A snapshot of the PV reveals the finescales associated with the instantaneous eddy field, the boundary forcing and midjet penetration (Fig. 11c). These PV distributions evolve as shown in a subsequent series of snapshots over the western flank of the basin in Fig. 12. They reveal bands of low and high PV induced by the frictional torques along the slope, as well as farther in the interior the opposing PV signals advected from the northern and southern boundaries. At the intergyre boundary, these PV contrast are advected into the interior. Subsequently, the plume of low PV undergoes a cycle of meanders and eddy formation and creation of narrow filaments (as shown in the time series in Fig. 12). The stirring associated with this process, and eventual dissipation on the scale of the grid cells, leads to the PV contrasts in the interior being much weaker than those on the boundary.

## 5. Discussion

Potential vorticity is a dynamical tracer that can be used to reveal the dominant dynamical balances within the ocean interior. For example, over the upper ocean, the PV distributions reflect a competition between ventilation from the surface mixed layer and eddy stirring. Over the mid depths and deep ocean, it is less clear how the PV is determined since fluid parcels might spend many years circulating before coming into contact with the mixed layer. Diabatic mixing is likely to play a role in determining the stratification and PV, given observations of enhanced mixing over boundaries (Armi 1978) and above rough topography (Polzin et al. 1997).

In our study, we extend the experiments of Hallberg and Rhines (2000) in investigating the role of sloping sidewalls in determining the PV distribution. A high resolution of  $\frac{1}{16}^\circ$  is incorporated along the shelf, and we examine the mechanism by which the PV is modified along the boundary. If there are vertical sidewalls, eddy stirring leads to PV homogenization within interior density layers. In contrast, if there are sloping sidewalls, frictional torques lead to bands of low and high PV being formed along the boundaries. For an idealized wind-driven, double gyre, the frictional bottom torque injects low PV over the subpolar gyre and high PV over the subtropical gyre. The separated jet along the intergyre boundary transfers these PV contrasts into the interior of the basin. Over a limited domain, this process can prevent eddy homogenization from occurring over the interior of the basin. In addition, enhanced diabatic mixing along the slope introduces low PV for inter-

mediate layers and can sometimes mask the frictional contribution.

Over a larger-scale domain, the injection of the PV contrasts formed from the bottom friction appears to be restricted to a subbasin scale. The eddy transfer of PV is sufficiently strong to erode and eventually remove the PV contrast, as well as the interior gyre circulation providing an opposing transfer of PV within the basin. Hence, the importance of this process depends on a number of factors: (i) the strength of the bottom flow and hence frictional drag, (ii) the relative magnitude of the PV contrast introduced by this frictional torque relative to the background PV contrast over the basin, (iii) whether the background circulation is sufficiently strong to transfer the PV contrasts from the boundary into the interior, and (iv) whether the eddies are sufficiently vigorous to erode this PV contrast and homogenize the interior. In addition, there is the possibility that the presence of more variable bottom topography might inhibit the process of eddy homogenization of PV (Merryfield and Holloway 1999; Adcock and Marshall 2000).

In terms of the observations, the frictional torques along the sidewalls do not appear to control the PV over the basin scale, which may be due to the weakness of the bottom flow, the lack of transfer of the PV anomaly into the interior, or eddies eroding the signature. Instead, there are extensive regions of nearly uniform PV over the thermocline of the North Atlantic and Pacific (McDowell et al. 1982; Keffer 1985), which are usually associated with eddy stirring. In addition, over the North Atlantic, there appears to be tight, eddy-driven deep circulations with PV homogenization (Lozier 1997). For deep and bottom waters, there are extensive pools of nearly uniform, low PV over northern abyssal basins with a poleward deep flow (O'Dwyer and Williams 1997); these signals can be explained in terms of the overturning circulation and diabatic mixing (Rousset et al. 2002; Williams et al. 2002). Frictional and diabatic processes along the sloping boundary might still play a role in determining the stratification and PV over the subbasin scale.

*Acknowledgments.* The work was supported by a UK NERC Research Grant GR3/119/55 and a HEFCE JREI award in 1999 for a supercomputing cluster (NESSC).

## APPENDIX

### Vorticity and PV Balances in MICOM

In MICOM, the momentum equation is written as

$$\begin{aligned} \frac{\partial \mathbf{u}}{\partial t} + \frac{\nabla u^2}{2} + (\zeta + f)\mathbf{k} \times \mathbf{u} + \nabla M \\ = -g \frac{\partial \tau}{\partial p} + \frac{1}{h} \nabla \cdot (v h \nabla \mathbf{u}), \end{aligned} \quad (\text{A1})$$

and the thickness equation is written as

$$\frac{\partial h}{\partial t} + \nabla \cdot (h\mathbf{u}) = B, \quad (\text{A2})$$

where  $B$  is the buoyancy forcing,  $g$  is gravity,  $h$  is the layer thickness,  $M$  is the Montgomery potential,  $p$  is pressure,  $\mathbf{u}$  is the horizontal velocity vector,  $\tau$  is the stress, and  $\nu$  is the diffusivity of momentum.

The vorticity equation is obtained from taking the vertical component of the curl of (A1):

$$\frac{\partial \zeta}{\partial t} + \nabla \cdot [(\zeta + f)\mathbf{u}] = -g \frac{\partial}{\partial p} (\mathbf{k} \cdot \nabla \times \boldsymbol{\tau}) + \mathbf{k} \cdot \nabla \times \left[ \frac{1}{h} \nabla \cdot (\nu h \nabla \mathbf{u}) \right]. \quad (\text{A3})$$

The layer version of the PV equation is obtained from combining (A2) and (A3):

$$\frac{D}{Dt} \left( \frac{\zeta + f}{h} \right) = -\frac{g}{h} \frac{\partial}{\partial p} (\mathbf{k} \cdot \nabla \times \boldsymbol{\tau}) + \frac{\mathbf{k}}{h} \cdot \nabla \times \left[ \frac{1}{h} \nabla \cdot (\nu h \nabla \mathbf{u}) \right] - \frac{(\zeta + f)B}{h^2}, \quad (\text{A4})$$

where  $D/Dt \equiv \partial/\partial t + \mathbf{u} \cdot \nabla$  is the substantial derivative.

In the limit of small gradients in  $h$  and  $\nu$ , (A4) can be written more concisely as

$$\frac{D}{Dt} \left( \frac{\zeta + f}{h} \right) = -\frac{g}{h} \frac{\partial}{\partial p} (\mathbf{k} \cdot \nabla \times \boldsymbol{\tau}) + \frac{\nu}{h} \nabla^2 \zeta - \frac{(\zeta + f)B}{h^2}. \quad (\text{A5})$$

Consequently, the PV is materially conserved apart from the forcing from (i) the vertical gradient in the stress, (ii) diffusion of vorticity, and (iii) layer thickness changes induced from buoyancy forcing. In most of the model integrations, the buoyancy forcing is taken simply as a biharmonic diffusion of thickness,  $B = -\nu_t \nabla^4 h$ , and  $\nu_t$  is the biharmonic diffusivity of thickness.

#### REFERENCES

- Adcock, S., and D. P. Marshall, 2000: Interactions between geostrophic eddies and the mean circulation over large-scale bottom topography. *J. Phys. Oceanogr.*, **30**, 3232–3238.
- Armi, L., 1978: Some evidence for boundary mixing in the deep ocean. *J. Geophys. Res.*, **83**, 1971–1979.
- Bleck, R., and L. T. Smith, 1990: A wind-driven isopycnic coordinate model of the North and Equatorial Atlantic Ocean. 1. Model development and supporting experiments. *J. Geophys. Res.*, **95**, 3273–3285.
- Ford, R., 2000: A baroclinic western boundary current over a continental slope. *J. Mar. Res.*, **58**, 327–373.
- Gargett, A. E., 1984: Vertical eddy diffusivity in the ocean interior. *J. Mar. Res.*, **42**, 359–393.
- Garrett, C., P. MacCready, and P. Rhines, 1993: Boundary mixing and arrested Ekman layers: rotating stratified flow near a sloping boundary. *Annu. Rev. Fluid Mech.*, **25**, 291–323.
- Hallberg, R., and P. B. Rhines, 2000: Boundary sources of potential vorticity in geophysical circulations. *Developments in Geophysical Turbulence*, R. M. Kerr and Y. Kimura, Eds., Kluwer, 51–65.
- Hughes, C. W., and B. A. De Cuevas, 2001: Why western boundary currents in realistic oceans are inviscid: A link between form stress and bottom pressure torques. *J. Phys. Oceanogr.*, **31**, 2871–2885.
- Keffer, T., 1985: The ventilation of the world's oceans: Maps of the potential vorticity field. *J. Phys. Oceanogr.*, **15**, 509–523.
- Lozier, M. S., 1997: Evidence for large-scale eddy-driven gyres in the North Atlantic. *Science*, **277**, 361–364.
- MacCready, P., and P. B. Rhines, 1993: Slippery bottom boundary layers on a slope. *J. Phys. Oceanogr.*, **23**, 5–22.
- McDowell, S., P. B. Rhines, and T. Keffer, 1982: North Atlantic potential vorticity and its relation to the general circulation. *J. Phys. Oceanogr.*, **12**, 1417–1436.
- Merryfield, W. J., and G. Holloway, 1999: Eddy fluxes and topography in stratified quasi-geostrophic models. *J. Fluid Mech.*, **380**, 59–80.
- Mertz, G., and D. G. Wright, 1992: Interpretations of the JEBAR term. *J. Phys. Oceanogr.*, **22**, 301–305.
- O'Dwyer, J., and R. G. Williams, 1997: The climatological distribution of potential vorticity over the abyssal ocean. *J. Phys. Oceanogr.*, **27**, 2488–2506.
- Phillips, O. M., 1970: On flows induced by diffusion in a stably stratified fluid. *Deep-Sea Res.*, **17**, 435–443.
- Polzin, K. L., J. M. Toole, J. R. Ledwell, and R. W. Schmitt, 1997: Spatial variability of turbulent mixing in the abyssal ocean. *Science*, **276**, 93–96.
- Rhines, P. B., 1998: Circulation, convection and mixing in rotating, stratified basins with sloping topography. *Physical Processes in Lakes and Oceans*, J. Imberger, Ed., AGU Coastal and Estuarine Studies, Vol. 54, Amer. Geophys. Union, 209–226.
- , and W. R. Holland, 1979: A theoretical discussion of eddy-driven mean flows. *Dyn. Atmos. Oceans*, **3**, 289–325.
- , and W. R. Young, 1982: Homogenization of potential vorticity in planetary gyres. *J. Fluid Mech.*, **122**, 347–368.
- Roussenov, V., R. G. Williams, and J. E. O'Dwyer, 2002: Formation of low potential vorticity over the deep Pacific. *J. Phys. Oceanogr.*, **32**, 1811–1823.
- Salmon, R., 1994: Generalized two-layer models of ocean circulation. *J. Mar. Res.*, **52**, 865–908.
- Williams, R. G., K. Day, V. Roussenov, and R. Woods, 2002: The role of the overturning circulation in determining the potential vorticity over the abyssal ocean. *J. Geophys. Res.*, **107**, 3170, doi:10.1029/2001JC001094.
- Wunsch, C., 1970: On oceanic boundary mixing. *Deep-Sea Res.*, **17**, 293–301.